

Unveiling the Electronic, Transport and Migration properties of the Te-defect lattice in DyTe_{1.8}

Jinwoong Kim^{1,*} and Nicholas Kioussis^{1,†}

¹*Department of Physics and Astronomy, California State University, Northridge, California 91330, USA*

(Dated: July 10, 2024)

The rare-earth ditellurides are known to form two-dimensional square lattice where the strong Fermi surface nesting leads to structural modulation. In contrast to charge density waves, the supercell modulation is accompanied by the formation of the periodic Te vacancy network, where the Te deficiency affects the nesting vector (i.e. the supercell size) via tuning the chemical potential. In this work, first principles electronic structure calculations for the $\sqrt{5} \times \sqrt{5}$ supercell, that commonly appears in this family of tellurides, unveil interesting electronic, transport, and migration properties of the Te defect lattice in DyTe_{1.8}. The reconstruction of the Te-deficient square lattice, consisting of a single Te-dimer and a pair Te-trimers per unit cell, gives rise to an out-of-plane polarization, whose direction depends on the position of the dimer. This results in various close-in-energy parallel and antiparallel polarization configurations of successive Te layers depending on the dimer positions. We predict that the orientation of the Te dimers, and hence the corresponding structural motifs, can be reversibly switched between two in-plane perpendicular directions under tensile epitaxial strain via a piezoelectric substrate, resulting in a colossal conductivity switching. Furthermore, the Te-dimer orientations result in asymmetric Fermi surface which can be confirmed by quantum oscillations measurements. Finally, we present numerical results for the migration paths and energy landscape through various divacancy configurations in the presence or absence of epitaxial strain.

I. INTRODUCTION

The rare-earth ditellurides $R\text{Te}_2$ (R represents a lanthanide element) are a family of layered materials renowned for a wide range of intriguing properties at low-temperature. These include charge density wave (CDW)[1, 2] magnetism,[3] superconductivity under high pressure,[4] as well as the simultaneous presence of CDW, superconductivity, and antiferromagnetism.[1] The unit cell of the crystal structure comprises of double-corrugated R -Te quasi-ionic layers separated by single planar square Te sheets stacked along the [001] direction, as illustrated in Fig. 1(a). From the electronic structure point of view, each $(R\text{-Te})^{1+}$ pair on the corrugated layer donates one electron to the Te atoms (Te_s) in the square plane.[5, 6]

In contrast to the rare earth tritellurides, $R\text{Te}_3$, which form stoichiometric compounds, the $R\text{Te}_{2-\delta}$ ($0.0 \lesssim \delta \lesssim 0.2$) compounds host Te_s vacancies on the Te_s square layer, giving rise to a wide range of structural motifs which depends sensitively on the Te deficiency δ and the rare earth cation.[7, 8] The Te_s vacancies effectively contribute extra charge to the layer which along with the isolated Te^{2-} anions form differently ordered patterns within the Te sheets. This results in superstructure modulations which can be commensurate with the parent structure, such as in $\text{CeSe}_{1.9}$ [9] and $\text{Gd}_8\text{Se}_{15}$ [10] structures, and incommensurate modulated structures such as $\text{DySe}_{1.84}$ [11] and $R\text{Se}_{1.84}$ ($R=\text{La-Nd, Sm}$)[12].

Recently, we have reported[7] experimental and first

principles electronic structure studies of the supercell formation in epitaxial $\text{DyTe}_{2-\delta}$ thin films, where for $\delta=0.2$ the modulation is a $(\sqrt{5} \times \sqrt{5})$ $R26.6^\circ \times 2$ superlattice. The superlattice emerges due to a periodic Te-defect lattice, which also acts to open a gap in the electronic spectrum and induces semiconducting transport behavior. First principles calculations point towards nesting conditions of the Fermi surface at a \mathbf{q} -vector that corresponds to the $\sqrt{5} \times \sqrt{5}$ condition, suggesting that the formation of the defect lattice results from a similar driving force to the conventional picture of CDW formation, where sections of the Fermi surface are gapped out by the formation of supercells with periodicity corresponding to the nesting condition[13]. Our total energy calculations[7] of the $\sqrt{5} \times \sqrt{5}$ supercell with Te_s mono- and divacancies in different configurations for $\delta = 0.1$ and 0.2 , showed that the second nearest-neighbor (SNN) vacancy configuration (denoted as the A-C configuration in Fig. 5c of Ref. [7]) has the lowest formation energy among the various considered structures, in agreement with previous X-ray diffraction measurements in $\text{SmTe}_{1.8}$. [14] The SNN di-vacancy configuration shown in Fig. 2(c), where the di-vacancies nucleate on sites 0 and 4 $\{0, 4\}$ in Fig. 2(a), consists of an ordered lattice of Te_s dimers and trimers.

Furthermore, first principles calculations of the $(\sqrt{5} \times \sqrt{5}) \times 2$ modulation along the c axis corresponding to the nucleation of a pair of A-C (0,4) divacancies on two Te square layers, reveals that the SNN A-C divacancy appears at a laterally displaced position (0.5, 0.5), relative to the divacancy on the adjacent Te square net layer. [7]

The objective of this work is to unveil the emergence of novel interesting properties of the periodic Te-defect lattice associated with the onset of ferroelectric polarization which depends sensitively on the position of the Te-dimer. In Sec. II we outline the methodology employed.

* jinwoong.kim@csun.edu

† nick.kioussis@csun.edu

In Sec. III we present results of (a) the position and orientation of the various Te-dimer configurations, (b) their polarization properties, (c) the electronic structure, (d) the Fermi surface anisotropy, (e) and (f) the transport and migration properties in the absence or presence of epitaxial strain. Conclusions are summarized in Sev. IV.

II. METHODOLOGY

The density functional theory calculations are performed using the Vienna *ab initio* simulation package (VASP)[15, 16] with the projector augmented wave method.[17, 18] The Dy-4*f* states are treated as core with valence configurations $5p^65d^16s^2$ and $5s^25p^4$ for Te. All structures are optimized using the PBEsol exchange correlation functional,[19] and the Bloch states are calculated and Wannierized[20, 21] with the modified Becke-Johnson potential[22, 23] which provides accurate band gaps, effective masses, and frontier-band ordering. The momentum space is sampled at a $80 \times 80 \times 80$ k-point mesh with the Wannier interpolation scheme. The conductivity is calculated using the semi-classical Boltzmann transport theory assuming a constant relaxation time. The tetrahedron method is employed to obtain the Fermi surface and its cross section area. In the polarization calculation, the topmost 51 valence bands are Wannierized for each spin channel where three and two *p* orbitals are initially projected on the Te_c and Te_s atoms, respectively, and five *s* orbitals are projected at the center of the Te-Te bonds in the square lattice. The integer ionic charges Z_n in Eq. 3 are +3 for Dy and +4 for Te atoms, respectively.

III. RESULTS AND DISCUSSION

A. Crystal structure

The crystal structure of pristine DyTe₂ is shown in Fig. 1(a), where the buckled DyTe slabs are separated by the planar Te square lattice that tends to undergo a supercell modulation whose periodicity interestingly depends on the Te vacancy concentration.[7, 8] The nesting function, $N(\mathbf{q})$, of the Fermi surface for an electron doping corresponding to the Te deficiency $\delta = 0.2$, reported in our recent calculations [Fig. S7(h) in Supporting information of Ref. [7]], is replotted in Fig. 1(b). It is zoomed-in near the \mathbf{q} point corresponding to the $\sqrt{5} \times \sqrt{5}$ modulation, marked as a cross point at (0.2, 0.4). Two strong peaks near the cross point, illustrated as dark orange colors, are traced as a function of doping which are displayed with the blue and green dots, where their separation increases with electron doping. The green peak is found to pass the cross point at higher Te deficient level ($\delta > 0.2$) that does not necessarily imply the need for additional Te vacancies, since the nesting function calculations involve several assumptions such as the rigid band approximation, constant matrix elements, and the

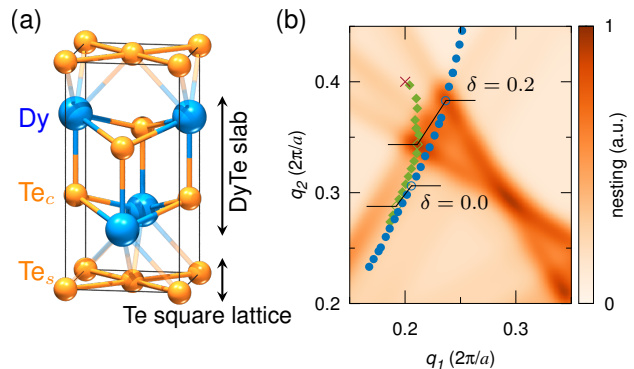


FIG. 1. (a) Unit cell of pristine DyTe₂ with two Te sites (Te_s) on the square net layer. (b) Calculated nesting function of DyTe₂. The back ground color map illustrates Gaussian-smearred nesting function for an electron doping level corresponding to Te deficiency, $\delta = 0.2$. The cross point indicates $\sqrt{5} \times \sqrt{5}$ wave vector. The two local nesting function peaks are marked with dots upon the doping level, that moves away from the origin with increasing electron doping.

exclusion of strain effect on the chemical potential. Our calculations demonstrate that the nesting function peaks associated with the formation of various supercell modulations change with chemical doping. Especially, the nesting function peaks (denoted by blue and green dots) approach the $\sqrt{5} \times \sqrt{5}$ modulation \mathbf{q} vectors with increasing Te deficiency in a good agreement with experiments.

Consequently, in this work we focus on the $\sqrt{5} \times \sqrt{5}$ modulation that commonly occurs for various rare-earth elements with two Te_s vacancies per modulated cell ($\delta = 0.2$)[7]. The in-plane lattice vectors of the supercell exhibiting chirality, shown in Fig. 2(a), are

$$\begin{pmatrix} \mathbf{a}_1^p \\ \mathbf{a}_2^p \end{pmatrix} = \begin{pmatrix} \frac{a_0}{\sqrt{2}}(\hat{x} - \hat{y}) \\ \frac{a_0}{\sqrt{2}}(\hat{x} + \hat{y}) \end{pmatrix} \quad \begin{pmatrix} \mathbf{a}_1^{s\pm} \\ \mathbf{a}_2^{s\pm} \end{pmatrix} = \begin{pmatrix} 2\mathbf{a}_1^p \pm \mathbf{a}_2^p \\ \mp \mathbf{a}_1^p + 2\mathbf{a}_2^p \end{pmatrix}, \quad (1)$$

where \mathbf{a}_i^p are the primitive lattice vectors and $\mathbf{a}_i^{s\pm}$ are two sets of supercell lattice vectors with \pm chirality. In general, a synthesized sample may have both types of domains leading to domain walls across which the chirality gets reversed. The two supercell structures with different chirality and their physical properties can be transformed to each other by a mirror operator, $\mathcal{M}_y : (x, y, z) \rightarrow (x, -y, z)$. Unless otherwise stated throughout the remainder of this manuscript we focus only the + chirality structure and ignore for convenience the superscript $s+$, namely, $\mathbf{a}_i \equiv \mathbf{a}_i^{s+}$.

The numerical indices in Fig. 2(a) represent the ten Te_s sites of the $\sqrt{5} \times \sqrt{5}$ supercell where the divacancy may be placed. The SNN divacancy (such as the $\{0, 4\}$, denoted as the A-C configuration in Ref. [7]) was found to have the lowest formation energy for the $\sqrt{5} \times \sqrt{5}$ modulation. The reconstructed square lattice consists of one Te-dimer and two Te-trimers per unit cell, resulting in several iso-energetic and ordered structural motifs. Fig-

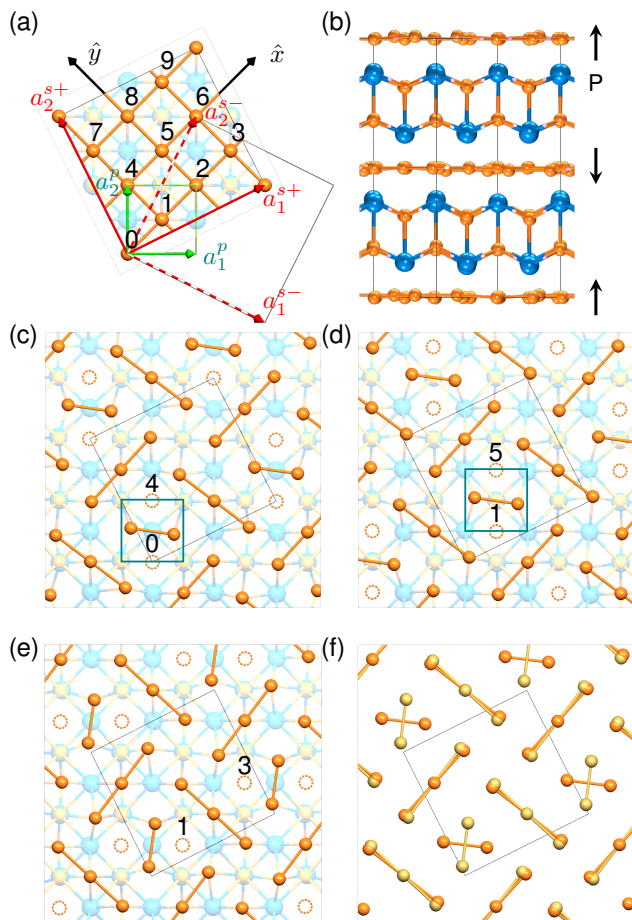


FIG. 2. Structural modulation of DyTe_2 . (a) Projection of the Te-square network on the (001) plane, where the numerical indices of the $\sqrt{5} \times \sqrt{5}$ -modulated cell denote the plausible positions of the Te_s divacancies. The \mathbf{a}_i^p are the primitive lattice vectors and $\mathbf{a}_i^{s\pm}$ are two sets of supercell lattice vectors with \pm chirality. (b) Side view of $\sqrt{5} \times \sqrt{5} \times 2$ modulated $\text{DyTe}_{1.8}$. Arrows depict the polarization configuration of individual Te square lattice layers in the ground state. (c-e) Reconstructed ordered Te-square network of $\text{DyTe}_{1.8}$ for several Te divacancy positions and orientations at the (c) $\{0,4\}$, (d) $\{1,5\}$, and (e) $\{1,3\}$ sites. Small squares in (c) and (d) denote the pristine cell enclosing the Te-dimer. (f) Mixed phase of the reconstructed Te-square network comprised of the structural motifs of (c) and (e), respectively, where the large square denotes the $\sqrt{5} \times \sqrt{5}$ cell.

ures 2(c) and (d) show the first and second structural motifs, associated with the $\{0,4\}$ and $\{1,5\}$ SNN divacancies, respectively, that look almost identical except for their positions relative to the DyTe slab. The thick squares in each panel emphasize the position of the Te_s dimers whose centers lie atop of the Dy (Te_c) atoms for the first (second) structural motif. The two structural motifs transform into each other through the mirror operation, \mathcal{M}_z , followed by a proper in-plane translation indicating a finite vertical polarization (see Fig. 3) whose sign depends on the position of the Te dimer, as will be

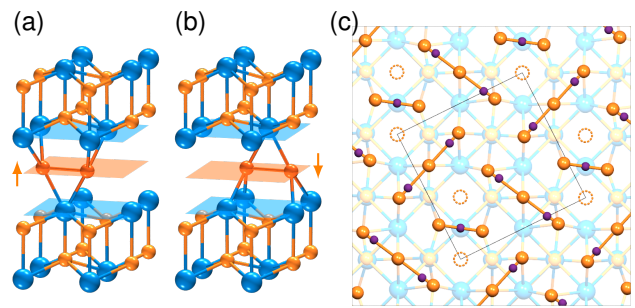


FIG. 3. Polarization of the Te square network. (a) Center of Te-dimer is atop of the Dy atom corresponding to the $\{0,4\}$ divacancy configuration. (b) Center of Te-dimer is atop of the Te atom corresponding to the $\{1,5\}$ divacancy configuration. The interlayer distances of the corrugated Dy-Te layers sandwiching the Te-dimer sheet are different. The Te-trimers are omitted for clarity. (c) Wannier charge centers lying on the covalent bonds, denoted by the purple dots on the reconstructed Te-square lattice for the $\{0,4\}$ divacancy configuration. The position of Wannier charge centers affects the polarization as well as the dipole moments.

discussed in the next section. The divacancy also reduces the \mathcal{C}_4 rotation symmetry of the pristine supercell to the \mathcal{C}_2 symmetry, whose rotational axis can be placed at the center of the Te dimer. The third structural motif associated with the $\{1,3\}$ divacancy can be transformed into the first motif of the $\{0,4\}$ divacancy through a \mathcal{C}_4 rotation, as illustrated in Figs. 2(c) and (e). The actual $\text{DyTe}_{1.8}$ samples may consist of a mixed phase of the $\{0,4\}$ - and $\{1,3\}$ -based structural motifs as shown in Fig. 2(f). The mixed phase can then preserve the tetragonal symmetry in macroscopic scale while the microscopic local domains are under uniaxial in-plane strain depending on the Te dimer orientation. This in turn raises an intriguing question whether an in-plane strain can align the orientation of the Te dimers, which is discussed in detail in Sec. III E.

In general, CDWs with a commensurate cell modulation of $n \times m$ can introduce nm distinct types of domains, associated with the relative translations of the modulated supercell. Therefore, there can be five different types of domains for the $\sqrt{5} \times \sqrt{5}$ modulation of $\text{DyTe}_{1.8}$. It is noteworthy that the three structural motifs discussed above do not transform into one another via lateral translation alone. The total number of distinct domains amounts to $2 \times 2 \times 5 = 20$, where the first (second) factor of 2 arises from the two possible positions (orientations) of the Te dimer in addition to the factor of 5 due to the lateral translations.

B. Polarization

The emergence of the $(\sqrt{5} \times \sqrt{5})$ superlattice induced by the periodic Te-vacant sites renders the $\text{DyTe}_{1.8}$ insulator.[7] The formation of the divacancy breaks the

TABLE I. Dipole moment and polarization of DyTe_{1.8} for the {0,4} divacancy along the supercell lattice vectors, \mathbf{a}_i , of the $\sqrt{5} \times \sqrt{5} \times 1$ cell.

	Dipole moment ($Q_e \mathbf{a}_i$)	Polarization (C/m ²)
\mathbf{a}_1	0.500	0.095
\mathbf{a}_2	0.500	0.095
\mathbf{a}_3	0.893	0.160

inversion symmetry which in turn results in finite polarization. Figures 3(a) and (b) clearly show the Dy-Te bonds of the Te_s dimers for the first and second structural motifs, which depend on their lateral position. Namely, in the first motif, where the center of the Te dimer is atop of the Dy atom, the dimer forms four (two) bonds with the Dy atoms on the upper (lower) layer, resulting in its proximity to the upper Dy-Te corrugated layer. Conversely, the second structural motif exhibits the opposite behavior.

The polarization \mathbf{p} and dipole moment \mathbf{d} of an insulator can be computed by considering the position of charged ions and Wannier charge centers (WCC) of the occupied Bloch states below the insulating band gap.[21, 24] As described in the methodology section, the topmost 51 valence bands are Wannierized which are well separated from both the semi-core states and the conduction bands. The Wannier functions are found exponentially localized near the initial position of projectors. Three and two Wannier functions are thus attached to Te_c and Te_s atoms, respectively. The positions of five interstitial Wannier functions, illustrated in Fig. 3(c), lie on the Te_s-Te_s bonds. The Wannier functions that deviate from the atomic sites render the system an obstructed atomic insulator.[25–28] The polarization and dipole moment are given by,

$$\mathbf{d} = \mathbf{p}V \quad (2)$$

$$= Q_e \left(\sum_n^{\text{ions}} Z_n (\mathbf{R}_n - \mathbf{r}_0) - \sum_n^{\text{WCC}} D (\mathbf{r}_n - \mathbf{r}_0) \right) \quad (3)$$

$$= Q_e \left(\sum_n^{\text{ions}} Z_n \mathbf{R}_n - \sum_n^{\text{WCC}} D \mathbf{r}_n - \mathbf{r}_0 \{N^+ - N^-\} \right) \quad (4)$$

$$= Q_e \left(\sum_n^{\text{ions}} Z_n \mathbf{R}_n - \sum_n^{\text{WCC}} D \mathbf{r}_n \right), \quad (5)$$

where V is the unit cell volume, Q_e is the electron charge, Z_n and \mathbf{R}_n are the ionic charge number and atomic position of the n -th atom, \mathbf{r}_n is the position of the n th WCC, and $D = 2$ is the spin degeneracy of the Wannier functions. The origin \mathbf{r}_0 does not affect the dipole moment as it is charge neutral, $N^+ = N^-$, where the net ionic charge, $N^+ = \sum_n^{\text{ions}} Z_n$ is equal to the number of WCCs, $N^- = D \sum_n^{\text{WCC}}$. Note that the WCC position, \mathbf{r}_n , can be shifted by integer multiples of lattice vectors, $\mathbf{r}_n \rightarrow \mathbf{r}_n + \sum_i m_i \mathbf{a}_i$ without affecting the physical observables that is associated with the gauge freedom leading

TABLE II. Calculated total energy of the $\sqrt{5} \times \sqrt{5} \times 2$ supercell for the lateral position, d , of the divacancy on the second Te layer relative to the first. The relative polarization directions of the two layers are labeled as P and AP for parallel and antiparallel configurations, respectively.

	Displacement of 2 nd layer, d					
	0	1	2	3	4	5
ΔE (meV/Dy)	0.0	-6.0	-8.4	-5.8	-7.3	-10.8
Polarization	P	AP	P	AP	P	AP

to the modulo definition of the modern theory of polarization. [29–31] The dipole moment is thus defined under modulo $DQ_e \mathbf{a}_i$ as long as the time reversal symmetry is preserved on the surface as well as in the bulk.

The calculated dipole moment and polarization of the first structural motif of the {0,4} divacancy, are listed in Table I. The \mathcal{C}_2 symmetry of the crystal structure confines the in-plane components of the dipole moments to be quantized[32] either to 0 or 1/2 in units of $Q_e \mathbf{a}_{1,2}$. The calculated in-plane dipole moments values of, 1/2, indicate nontrivial Zak phase[32] of DyTe_{1.8} in the $\sqrt{5} \times \sqrt{5} \times 1$ supercell that induces metallic (side) surfaces due to the emergent in-gap states. We note that the physical samples, however, exhibit additional $\times 2$ structural modulation along the \hat{z} direction[7] resulting in $\sqrt{5} \times \sqrt{5} \times 2$ supercell which cancels out the in-plane dipole moment. The concept of quantized polarization under crystal symmetry was first elucidated by Zak[32] and has recently been integrated into the framework of topological insulators.[30, 33–35]

This additional modulation also controls the net dipole moment along the \hat{z} direction as each layer may have upward or downward dipole moment depending on the position of the Te_s dimers of each layer. In our previous study,[7] the total energy of the $\sqrt{5} \times \sqrt{5} \times 2$ supercell was calculated (see Table II) for various pairs of divacancy configurations, $\{0, 4\} - \{d, d + 4\}$, $d = \{0, 1, 2, 3, 4, 5\}$ where the first divacancy nucleates at sites $\{0, 4\}$ on the first Te_s layer while the second pair nucleates on sites $\{d, d + 4\}$ on the second Te_s layer. The supercell structure with $d = 5$ is found to exhibit the lowest energy in which the polarization direction of the upper layer is opposite to that of the lower layer as illustrated in Fig. 2(b). The next stable structure with $d = 2$ has 2.4 meV/Dy higher total energy and the polarization directions of the two layers are parallel leading to finite net polarization, suggesting that an out-of-plane external electric field, $E \gtrsim 15$ MV/m may stabilize the polarized structure.

C. Electronic structure - Van Hove singularities

Figure 4 shows the calculated electronic structure of DyTe_{1.8} with the {0,4} divacancy configuration. In

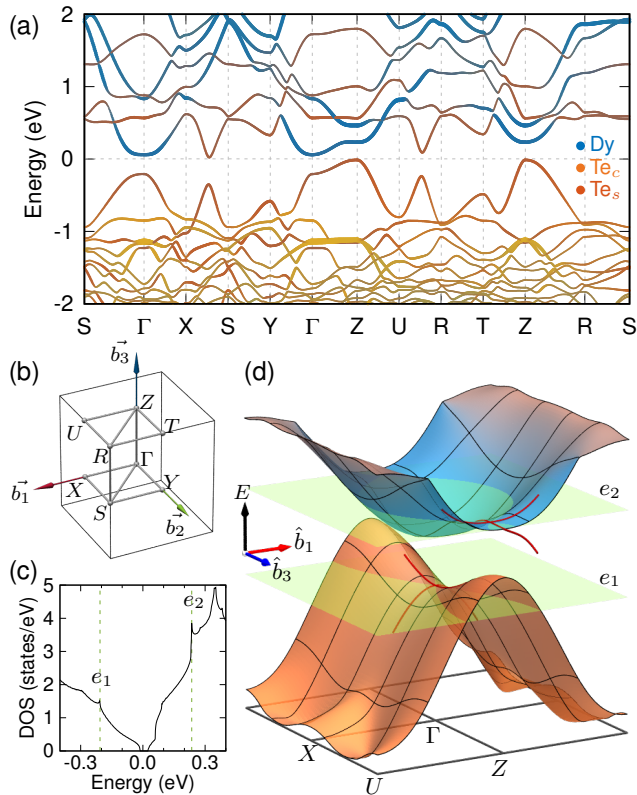


FIG. 4. Calculated electronic structure of $\text{DyTe}_{1.8}$ and Van Hove singularities near the Fermi level. (a) Band structure of the $\{0, 4\}$ divacancy configuration along high symmetry lines. (b) BZ of the $\sqrt{5} \times \sqrt{5}$ -modulated supercell and the high symmetry points. Van Hove singularities near the Fermi level. (c) Calculated DOS near the Fermi level showing the emergence of Van Hove singularities at the energies, e_1 and e_2 , of the saddle points in both the hole and electron doped regimes. (d) Two dimensional band structure on the $\hat{b}_1 - \hat{b}_3$ plane, where the orange and blue colors denote the Te_s - p and Dy - d orbital characters, respectively. Valence (conduction) band exhibits saddle point(s) at the Γ (near the Z) point marked with red curves. The energy levels, e_1 and e_2 , of the saddle points are illustrated with transparent planes.

Fig. 4(b) we plot the Brillouin zone (BZ) of the $\sqrt{5} \times \sqrt{5}$ -modulated cell of $\text{DyTe}_{1.8}$ with the high symmetry directions used in the band structure plot. The blue, red and orange colors denote projections on the Dy - d , Te_s - p , and Te_c - p orbitals. The indirect (direct) band gap is 0.14 (0.33) eV in qualitative agreement with the activation gap measured in transport.[7]

In our previous study[7] of the electronic structure of pristine DyTe_2 , we found that the Te_s - p bands, originating from the square lattice, intersect the Fermi level and give rise to the nesting peaks near the \mathbf{q} vectors corresponding to the $\sqrt{5} \times \sqrt{5}$ cell modulation. These nesting peaks explain the cell modulation and resulting insulating band gap in $\text{DyTe}_{1.8}$, which is further enhanced by the formation of the vacancy network, which increases the inter-nested-states coupling strengths. The topmost va-

lence band of $\text{DyTe}_{1.8}$ retains the 2D nature of the square lattice, with highly dispersive bands along the in-plane direction and weakly dispersive bands along the out-of-plane direction such as the $\Gamma - Z$ and $R - S$ symmetry lines. The dimensional reduction in the band structure likely introduces saddle points, leading to Van Hove singularities (VHS). Figure 4(d) illustrates the saddle points on the $\hat{b}_1 - \hat{b}_3$ plane and the corresponding divergent peaks of the density of states (DOS). The conduction band, dominated by the Dy - d orbital character, also exhibits saddle points on this plane which slightly deviate from the Z point by $\pm 0.1\hat{b}_3$. These VHS in both the valence and conduction bands are expected to give rise to significant optical responses due to the high joint DOS, where the energy difference, $e_2 - e_1 = 0.44$ eV, corresponds to the infrared wavelength, $\lambda = 2.8 \mu\text{m}$. However, these saddle points are separated in momentum space, necessitating a phonon coupling to complement the momentum difference, $\Delta k_z \sim 0.4|\hat{b}_3|$. Fortunately, the system undergoes another double cell modulation along the \hat{z} direction, which in turn folds the Z point to the Γ point. Thus, in the long-wavelength limit, optical absorption between the two saddle points can occur without phonon assistance. Additionally, the vertical polarization of each square lattice layer induces a Rashba spin splitting in the presence of spin-orbit coupling. The alignment of these layers' polarizations determines the spin texture chirality of the spin-split bands, influencing the band alignment and consequent optical responses. Further theoretical and experimental investigations are needed to fully understand these effects.

D. Electronic structure - Fermi surface

Figures 5(a)-(e) display the calculated 3D Fermi surface (FS) sheets and their (001) projections, of $\text{DyTe}_{1.8}$ with the $\{0, 4\}$ divacancy configuration for chemical potential shifts, $\mu = E - E_F$, ranging from (a) +0.3 eV to (e) -0.5 eV in steps of 0.2 eV. The orange and blue colors denote the Te_s - p and Dy - d orbital characters, respectively. For $\mu = -0.5$ eV the chemical potential lies in the Te_s - p -derived valence bands [see Fig. 4(a)], and the FS consists of highly-nested parallel sheets stacked normal to the Γ - S symmetry direction of the BZ [Fig. 4(b)]. As the chemical potential shifts upward in energy, the FS area gradually gets reduced and isolated pockets appear at Z point. Above the Fermi level, two elongated electron pockets emerge on the side surface of the BZ as shown in Fig. 5(b) and eventually a Dy - d derived electron pocket emerges at Γ point [Fig. 5(a)]. In Fig. 5(f) we display the FS sheets and their (001) projections for the $\{1, 3\}$ divacancy configuration for $\mu = -0.5$ eV. Comparison of Figs. 5(e) and (f) clearly shows the 90° rotation of the FS associated with the Te_s dimer rotation by 90° about $[001]$, shown in Fig. 2(e). Since the group velocity is always normal to the FS, the parallel FS sheets indicate 1D conducting channels where their direction can

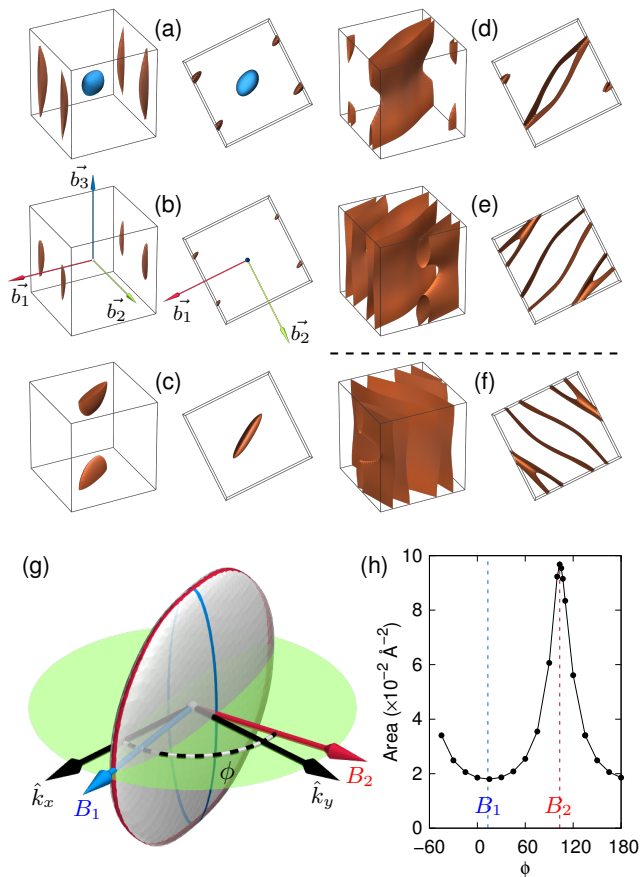


FIG. 5. Asymmetric Fermi surface (FS) sheets (left columns) and their (001) projections (right columns), of $\text{DyTe}_{1.8}$ with the $\{0,4\}$ divacancy configuration for chemical potential shifts, $\mu = E - E_F$, ranging from (a) +0.3 eV to (e) -0.5 eV in steps of 0.2 eV. Orange and blue colors denote the Te_s - p and Dy- d orbital characters, respectively. (f) FS sheets (left panel) and their (001) projections (right panel) for the $\{1,3\}$ divacancy configuration for $\mu = -0.5$ eV. (g) Fermi surface at $\mu = -0.1$ eV. Green circular area shows the $\hat{k}_x - \hat{k}_y$ plane on which the external magnetic field is swept with an azimuthal angle ϕ from the \hat{k}_x axis. The corresponding maximal cross-section paths under the external field along B_1 and B_2 are illustrated with blue and red stripes, respectively, on the Fermi surface. (h) Calculated maximal cross-section area versus ϕ .

be switched by the Te dimer orientations, that will be discussed in the next section.

As alluded above, the valence bands are dominated by the Te_s atoms of the 2D square lattice. The Te-dimer orientations switch the hopping directions within the square lattice that further refine the 2D like band structure into an effective 1D channel resulting in asymmetric Fermi surface as shown in Fig. 5. The FS asymmetry can be confirmed by measuring the quantum oscillations under external magnetic field whose frequency provides information of the maximal cross-section area of the FS. Figure 5(g) shows the disk shape Fermi surface centered at

the Z point under hole doping for $\mu = -0.1$ eV. The maximal cross-section area shown in Fig. 5(h) is expected to strongly depend on the magnetic field direction, where a peak appears at the azimuthal angle (measured from \hat{k}_x), $\phi \sim 103^\circ$, corresponding to B_2 . The red stripe on the Fermi surface shows the cyclotron motion path under the external field B_2 while the blue stripe is under B_1 whose cross-section area is smaller than that of B_2 by a factor of five.

E. Quasi 1D conducting channel

The results of the various reconstructed iso-energetic divacancy configurations invite the intriguing question whether epitaxial strain, which is ubiquitous in $\text{DyTe}_{1.8}$ samples grown on atomically flat piezoelectric substrates, shown schematically in Fig. 6(a), can stabilize a specific ordered structural motif, and whether the divacancy configuration network can undergo a transition from one motif to another. Fig. 6(b) shows the landscape of the total energy difference, $\Delta E = E(\{0,4\}) - E(\{1,3\})$, between the $\{0,4\}$ - and $\{1,3\}$ divacancy structural motifs of the $\sqrt{5} \times \sqrt{5}$ reconstructed $\text{DyTe}_{1.8}$ on the two-dimensional epitaxial strain, $r_x \equiv \frac{\alpha_x}{\alpha_0}$ and $r_y \equiv \frac{\alpha_y}{\alpha_0}$. Here, α_0 is the in-plane equilibrium lattice constant of the square lattice, and the x and y refer to the $[110]$ and $[\bar{1}10]$ directions, respectively. The calculations reveal that tensile epitaxial strain, $\epsilon_{yy} \approx 0.7\%$, renders the $\{0,4\}$ divacancy-based configuration as the ground state [Fig. 6(c)]. On the other hand, the $\{1,3\}$ divacancy-based structural motif becomes the ground state under tensile strain, $\epsilon_{xx} \approx 0.7\%$ along $[110]$ [Fig. 6(d)]. Interestingly, these two distinct Te_s -vacancy ordered networks have substantial different transport properties. Figure 6(e) shows the matrix elements of the longitudinal conductivity, σ_{ii} ($i=x,y,z$), of $\text{DyTe}_{1.8}$ with the $\{0,4\}$ divacancy configuration versus the chemical potential, μ . The conductivity ratio, $\frac{\sigma_{yy}}{\sigma_{xx}}$ versus μ is also plotted as a dashed line whose scale appears on the right vertical axis. Interestingly, σ_{yy} , is higher by more than one order of magnitude compared to σ_{xx} under hole doping.

This notable conductivity switching between the two phases upon the Te dimer orientation, suggests potential application as a memory device. Control of the dimer orientation can be achieved by applying epitaxial strain via a piezoelectric substrate, which can in turn align all or most of the sample's Te dimers along the \hat{x} or \hat{y} directions, resulting in a colossal conductivity contrast, ranging from 1000% to 2500% between the ON and OFF phases.

Consequently, the Te dimer in the supercell acts as a molecular switch not only in a macroscopic scale but also in a microscopic level by controlling the electron hopping directions within the $\sqrt{5} \times \sqrt{5}$ supercell. The overall conductivity of the two-dimensional percolation network[36, 37] will be determined by the microscopic configurations of the Te dimer orientations, which can

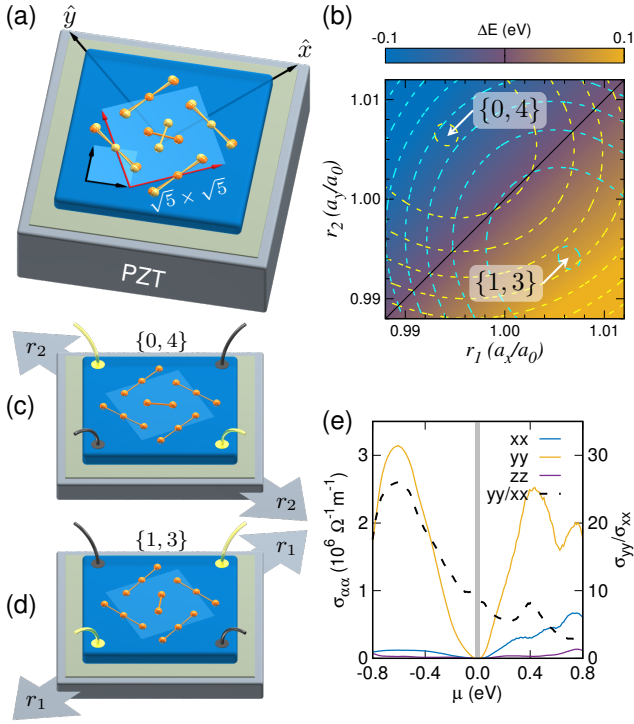


FIG. 6. Effect of uniaxial in-plane strain on Te-dimer orientation. (a) Schematic figure of $\text{DyTe}_{1.8}$ epitaxially grown on a piezoelectric substrate. Small (large) square shows the in-plane unit cell of primitive DyTe_2 ($\sqrt{5} \times \sqrt{5}$ -modulated $\text{DyTe}_{1.8}$) structure. (b) Landscape of total energy difference, $\Delta E = E(\{0,4\}) - E(\{1,3\})$, between the $\{0,4\}$ - and $\{1,3\}$ divacancy structural motifs of the $\sqrt{5} \times \sqrt{5}$ supercell on two-dimensional epitaxial strain, $r_x \equiv \frac{\alpha_x}{\alpha_0}$ and $r_y \equiv \frac{\alpha_y}{\alpha_0}$. Yellow and blue dashed curves indicate energy contours of the $\{0,4\}$ and $\{1,3\}$ phases, respectively. (c) and (d) Relatively stable Te-dimer orientations under uniaxial strain. The $\{0,4\}$ ($\{1,3\}$) phase is preferred under uniaxial strain along the \hat{y} (\hat{x}) direction. Gold (black) leads indicate higher (lower) conductivity channel. (e) Calculated conductivity of $\text{DyTe}_{1.8}$ with the two vacancies at $\{0,4\}$ versus the chemical potential μ . Conductivity along \hat{y} [see (a) or Fig. 2(a) for the direction] is higher more than one order of magnitude compared to the other directions under hole doping. The dashed line denotes the in-plane conductivity ratio, σ_{yy}/σ_{xx} . The band gap near $\mu = 0$ is marked with the gray box.

be tuned by epitaxial strain. We acknowledge the significance of prior nanotube percolation experiments[38, 39], particularly those where the nanotube orientation was controllable, which garnered considerable attention within the research community. Given the potential for strain-controlled dimer orientations, $\text{DyTe}_{1.8}$ emerges as a promising alternative platform for conducting percolation experiments.

F. Migration Properties

In order to understand the diffusion properties of the divacancy configurations in the presence or absence of epitaxial strain, we have carried first principles calculations using the nudged elastic band (NEB) method[40–43] to determine the energy barriers and the minimum energy paths associated with the atomic migrations within the Te square network. The energy saddle point identified by this method represents the barrier between two stable configurations and the migration is assumed to occur simultaneously across all periodic (both in-plane and out-of-plane) cells, rendering the calculated energy barrier an upper bound. Consequently, the energy required to incrementally expand a domain area could be less than the barrier determined by this method.

There are numerous atomic migration paths, some of which are symmetric equivalents with identical energy barriers. Therefore, only four irreducible migration paths require computation which collectively represent all possible migrations. The eight dotted arrows depicted in the Fig. 7(a), (b), (e), and (f) represent these four migration paths (colored red, green, cyan, and purple) adjacent to the vacant sites. Paths of the same color are reverse equivalents of each other. A pairwise combination of these migrations can describe both polarization reversal and dimer rotation.

For instance, the migration from (a) $\{5,9\}$ to (b) $\{5,6\}$ to (c) $\{2,6\}$ changes the position of the dimer and thus the polarization direction. In the first step, the right side Te of a dimer moves to the vacant site, denoted by the red dotted arrow in Fig. 7(a) where the intermediate positions of the Te atom are illustrated as transparent red spheres in Fig. 7(b). Next, the middle Te of a trimer moves upwards, marked as red dotted arrow in Fig. 7(b) that completes the migration path to the opposite polarization [Fig. 7(c)]. If the second step migration is replaced by the purple dotted arrow [Fig. 7(b)] where the end Te atom moves instead of the middle one of the trimer, it arrives to the (d) $\{3,5\}$ configuration exhibiting opposite polarization and rotated dimer orientation compared to the initial state (a) $\{5,9\}$.

The calculated energies during each migration step are shown in Fig. 7(i) where the red (purple) colored line corresponds to the migration marked with the red (purple) arrows with an energy barrier of 0.75 eV (0.37 eV). The horizontal axis is for images in the NEB method between stable configurations listed below the ticks. The possible migration paths between the configurations are denoted as colored lines connecting them. For an instance, migrations from (e) $\{6,8\}$ to (f) $\{5,8\}$ to (a) $\{5,9\}$ are connected by cyan and green lines below Fig. 7(i) corresponding to the energy curves colored cyan and green, respectively.

We note that the previously considered polarization reversal migration, $\{5,9\} - \{5,6\} - \{2,6\}$ takes the red energy curves back and forth passing the 0.75 eV energy barrier twice. The Te-dimer then moves towards the $-\hat{y}$

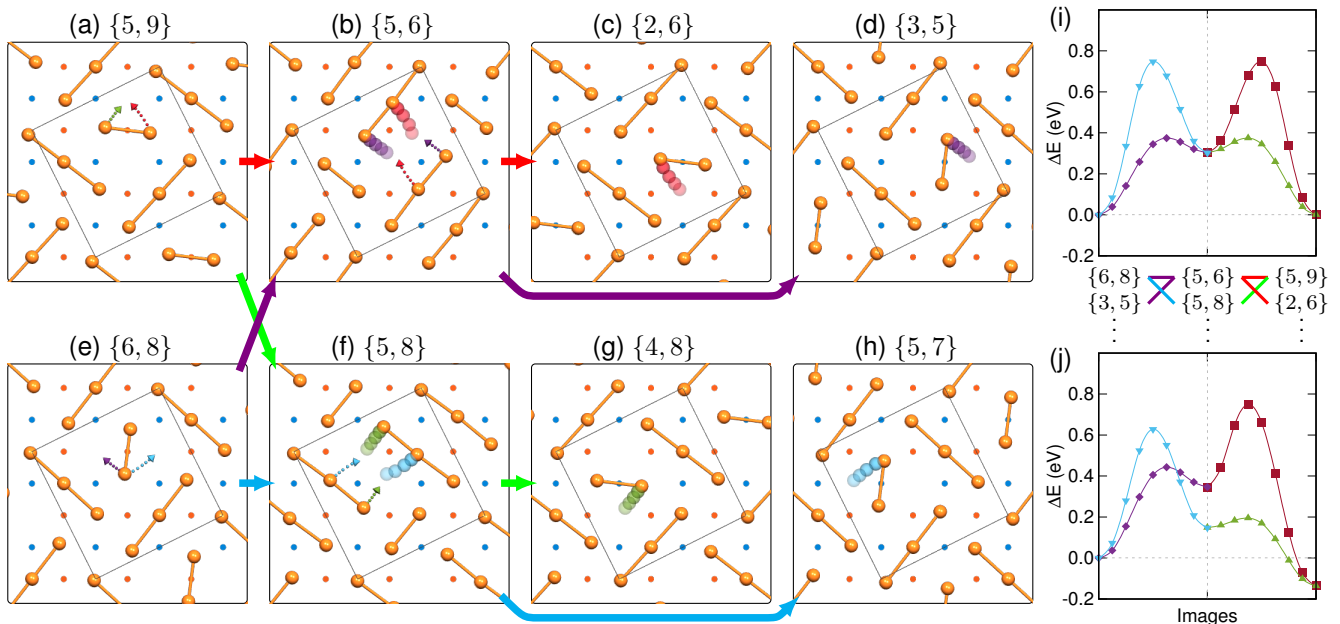


FIG. 7. (a-h) Te-square net with various di-vacancy configurations and their migrations. Background blue (orange) dots denote the positions of Dy (Te_c) atoms below the Te-square net layer. Arrows illustrate the considered paths of ionic migrations. Four different types of migration paths are colored by red, green, cyan, and violet. (i,j) Calculated migration energy landscape of the various transitions for (i) symmetric, $r_1 = r_2 = 1.0$ and (j) asymmetric, $r_1 = 0.988$, $r_2 = 1.012$, in-plane strain.

direction. The polarization can be reversed by another migration of $\{5,9\} - \{5,8\} - \{4,8\}$ towards the $-\hat{x}$ direction that needs to overcome the green energy curves passing the 0.37 eV barrier twice instead. The latter one experiences a lower energy barrier indicating that there is a preferred direction in the dimer migration which is determined by the supercell chirality and the dimer orientation.

The migration energies are considered within square symmetry, where pairs of paths exhibit the same energy barrier. Figure 7 (j) shows the change of the migration energy landscape under uniaxial strain $r_2 > r_1$ (see the caption). The previously degenerate total energies of the ground-state divacancy configurations are lifted, and the $\{5,9\}$ configuration becomes more stable than the $\{6,8\}$ due to distinct Te-dimer orientations. Additionally, the metastable $\{5,8\}$ configuration becomes more stable than its $\{5,6\}$ counterpart.

IV. SUMMARY

The structural and electronic properties of $\text{DyTe}_{1.8}$ are investigated by employing first-principles calculations. In addition to the $\sqrt{5} \times \sqrt{5}$ modulation, the detailed posi-

tion and orientation of the Te dimers are found to play a crucial role in determining the polarization and the electronic structure near the Fermi level. The predicted small insulating gap with VHS in both the valence and conduction bands imply characteristic optical responses with fine structures related with the polarization direction of each Te square lattice layer. The Te-dimer-orientation-induced asymmetric Fermi surface may be directly confirmed by quantum oscillation measurements and paves a way to memory device application with mechanically switchable quasi one-dimensional conductivity. Finally, the ionic migration paths and energy landscape results reveal a plethora of structural transitions between isoenergetic motifs. Our predictions of these interesting and diverse properties of $\text{DyTe}_{1.8}$ will hopefully motivate further experimental and theoretical investigations.

ACKNOWLEDGMENTS

We appreciate insightful discussions with Joseph Falson and Adrian Llanos. The work is supported by the NSF-PREP CSUN/Caltech-IQIM Partnership (grant number 2216774) and the NSF-Partnership in Research and Education in Materials (PREM) (grant number DMR-1828019).

[1] K. Y. Shin, V. Brouet, N. Ru, Z. X. Shen, and I. R. Fisher, Electronic structure and charge-density wave for-

mation in $\text{LaTe}_{1.95}$ and $\text{CeTe}_{2.00}$, Phys. Rev. B **72**,

- 085132 (2005).
- [2] D. R. Garcia, G.-H. Gweon, S. Y. Zhou, J. Graf, C. M. Jozwiak, M. H. Jung, Y. S. Kwon, and A. Lanzara, Revealing charge density wave formation in the LaTe_2 system by angle resolved photoemission spectroscopy, *Phys. Rev. Lett.* **98**, 166403 (2007).
 - [3] Y. Shin, C. Han, B. Min, H. Lee, C. Choi, Y. Kim, D. Kim, and Y. Kwon, Anisotropic magnetization in $R\text{Te}_2$ (R : Ce, Pr, Gd and Sm), *Physica B: Condensed Matter* **291**, 225 (2000).
 - [4] M. H. Jung, A. Alsmadi, H. C. Kim, Y. Bang, K. H. Ahn, K. Umeo, A. H. Lacerda, H. Nakotte, H. C. Ri, and T. Takabatake, Superconductivity in magnetically ordered $\text{CeTe}_{1.82}$, *Phys. Rev. B* **67**, 212504 (2003).
 - [5] W. Tremel and R. Hoffmann, Square nets of main-group elements in solid-state materials, *Journal of the American Chemical Society* **109**, 124 (1987).
 - [6] A. Kikuchi, Electronic structure of lanthan ditellurides, *Journal of the Physical Society of Japan* **67**, 1308 (1998), <https://doi.org/10.1143/JPSJ.67.1308>.
 - [7] A. Llanos, S. Salmani-Rezaie, J. Kim, N. Kiuoussis, D. A. Muller, and J. Falson, Supercell formation in epitaxial rare-earth ditelluride thin films, *Crystal Growth & Design* **24**, 115 (2024).
 - [8] H. Poddig, P. Gebauer, K. Finzel, K. Stöwe, and T. Doert, Structural variations and bonding analysis of the rare-earth metal tellurides $RE\text{Te}_{1.875\pm\delta}$ ($RE = \text{Ce, Pr, Sm, Gd}$; $0.004 \leq \delta \leq 0.025$), *Inorganic Chemistry* **60**, 11231 (2021).
 - [9] P. Plambeck-Fischer, W. Abriel, and W. Urland, Preparation and crystal structure of $RE\text{Se}_{1.9}$ ($RE = \text{Ce, Pr}$), *Journal of Solid State Chemistry* **78**, 164 (1989).
 - [10] E. Dashjav, O. Oeckler, T. Doert, H. Matyjasch, and P. Böttcher, $\text{Gd}_8\text{Se}_{15}$ —A 24-fold superstructure of the ZrSSi type, *Angewandte Chemie International Edition* **39**, 1987 (2000), <https://onlinelibrary.wiley.com/doi/pdf/10.1002/1521-3773>.
 - [11] A. van der Lee, L. M. Hoistad, M. Evain, B. J. Foran, and S. Lee, Resolution of the 66-fold superstructure of $\text{DySe}_{1.84}$ by x-ray diffraction and second-moment scaled hückel calculations, *Chemistry of Materials* **9**, 218 (1997).
 - [12] C. Graf and T. Doert, $\text{LaSe}_{1.85}$, $\text{CeSe}_{1.83}$, $\text{NdSe}_{1.83}$ and $\text{SmSe}_{1.84}$ – four new rare earth metal polyselenides with incommensurate site occupancy and displacive modulation, *Zeitschrift für Kristallographie* **224**, 568 (2009).
 - [13] S. Lee and B. J. Foran, Defective lattice charge density waves in $\text{La}_{10}\text{Se}_{19}$, $\text{Cs}_3\text{Te}_{22}$, RbDy_3Se_8 , and $\text{Dy}_{65.33}\text{Se}_{120}$, *Journal of the American Chemical Society* **118**, 9139 (1996).
 - [14] I. Ijjaali and J. A. Ibers, Two new binary lanthanide polytellurides: Syntheses and crystal structures of $\text{CeTe}_{1.90}$ and $\text{SmTe}_{1.80}$, *Journal of Solid State Chemistry* **179**, 3456 (2006).
 - [15] G. Kresse and J. Furthmüller, Efficient iterative schemes for *ab initio* total-energy calculations using a plane-wave basis set, *Phys. Rev. B* **54**, 11169 (1996).
 - [16] G. Kresse and J. Furthmüller, Efficiency of *ab-initio* total energy calculations for metals and semiconductors using a plane-wave basis set, *Computational Materials Science* **6**, 15 (1996).
 - [17] P. E. Blöchl, Projector augmented-wave method, *Phys. Rev. B* **50**, 17953 (1994).
 - [18] G. Kresse and D. Joubert, From ultrasoft pseudopotentials to the projector augmented-wave method, *Phys. Rev. B* **59**, 1758 (1999).
 - [19] J. P. Perdew, A. Ruzsinszky, G. I. Csonka, O. A. Vydrov, G. E. Scuseria, L. A. Constantin, X. Zhou, and K. Burke, Restoring the density-gradient expansion for exchange in solids and surfaces, *Phys. Rev. Lett.* **100**, 136406 (2008).
 - [20] A. A. Mostofi, J. R. Yates, G. Pizzi, Y.-S. Lee, I. Souza, D. Vanderbilt, and N. Marzari, An updated version of wannier90: A tool for obtaining maximally-localised wannier functions, *Comput. Phys. Commun.* **185**, 2309 (2014).
 - [21] N. Marzari, A. A. Mostofi, J. R. Yates, I. Souza, and D. Vanderbilt, Maximally localized Wannier functions: Theory and applications, *Rev. Mod. Phys.* **84**, 1419 (2012).
 - [22] A. D. Becke and E. R. Johnson, A simple effective potential for exchange, *The Journal of Chemical Physics* **124**, 10.1063/1.2213970 (2006), 221101, https://pubs.aip.org/aip/jcp/article-pdf/doi/10.1063/1.2213970/15385734/221101_1_online.pdf.
 - [23] F. Tran and P. Blaha, Accurate band gaps of semiconductors and insulators with a semilocal exchange-correlation potential, *Phys. Rev. Lett.* **102**, 226401 (2009).
 - [24] J. Kim, K. M. Rabe, and D. Vanderbilt, Negative piezoelectric response of van der waals layered bismuth tellurohalides, *Phys. Rev. B* **100**, 104115 (2019).
 - [25] H. C. Po, H. Watanabe, and A. Vishwanath, Fragile topology and wannier obstructions, *Phys. Rev. Lett.* **121**, 126402 (2018).
 - [26] S. K. Radha and W. R. L. Lambrecht, Topological obstructed atomic limit insulators by annihilating dirac fermions, *Phys. Rev. B* **103**, 075435 (2021).
 - [27] X.-P. Li, D.-S. Ma, C.-C. Liu, Z.-M. Yu, and Y. Yao, From atomic semimetal to topological nontrivial insulator, *Phys. Rev. B* **105**, 165135 (2022).
 - [28] Y. Xu, L. Elcoro, Z.-D. Song, M. G. Vergniory, C. Felser, S. S. P. Parkin, N. Regnault, J. L. Mañes, and B. A. Bernevig, Filling-enforced obstructed atomic insulators, *Phys. Rev. B* **109**, 165139 (2024).
 - [29] R. D. King-Smith and D. Vanderbilt, Theory of polarization of crystalline solids, *Phys. Rev. B* **47**, 1651 (1993).
 - [30] D. Vanderbilt and R. D. King-Smith, Electric polarization as a bulk quantity and its relation to surface charge, *Phys. Rev. B* **48**, 4442 (1993).
 - [31] R. Resta, Macroscopic polarization in crystalline dielectrics: the geometric phase approach, *Rev. Mod. Phys.* **66**, 899 (1994).
 - [32] J. Zak, Berry's phase for energy bands in solids, *Phys. Rev. Lett.* **62**, 2747 (1989).
 - [33] Y. Aihara, M. Hirayama, and S. Murakami, Anomalous dielectric response in insulators with the π zak phase, *Phys. Rev. Research* **2**, 033224 (2020).
 - [34] M. Smeu, H. Guo, W. Ji, and R. A. Wolkow, Electronic properties of $\text{si}(111)\text{-}7 \times 7$ and related reconstructions: Density functional theory calculations, *Phys. Rev. B* **85**, 195315 (2012).
 - [35] J. Kim, C.-Y. Huang, H. Lin, D. Vanderbilt, and N. Kiuoussis, Bismuth antiphase domain wall: A three-dimensional manifestation of the su-schrieffer-heeger model, *Phys. Rev. B* **107**, 045135 (2023).
 - [36] M. Sahimi, *Application of Percolation Theory*, Vol. 213 (SpringerCham, 2023) pp. XXI,680.

- [37] V. A. Cherkasova, Y. Y. Tarasevich, N. I. Lebovka, and N. V. Vygornitskii, Percolation of aligned dimers on a square lattice, *The European Physical Journal B* **74**, 205 (2010).
- [38] F. Du, J. E. Fischer, and K. I. Winey, Effect of nanotube alignment on percolation conductivity in carbon nanotube/polymer composites, *Phys. Rev. B* **72**, 121404(R) (2005).
- [39] C. Park, J. Wilkinson, S. Banda, Z. Ounaies, K. E. Wise, G. Sauti, P. T. Lillehei, and J. S. Harrison, Aligned single-wall carbon nanotube polymer composites using an electric field, *Journal of Polymer Science Part B: Polymer Physics* **44**, 1751 (2006).
- [40] G. Mills, H. Jónsson, and G. K. Schenter, Reversible work transition state theory: application to dissociative adsorption of hydrogen, *Surface Science* **324**, 305 (1995).
- [41] H. Jónsson, G. Mills, and K. W. Jacobsen, Nudged elastic band method for finding minimum energy paths of transitions, in *Classical and Quantum Dynamics in Condensed Phase Simulations*, pp. 385–404.
- [42] G. Henkelman, B. P. Uberuaga, and H. Jónsson, A climbing image nudged elastic band method for finding saddle points and minimum energy paths, *The Journal of Chemical Physics* **113**, 9901 (2000).
- [43] G. Henkelman and H. Jónsson, Improved tangent estimate in the nudged elastic band method for finding minimum energy paths and saddle points, *The Journal of Chemical Physics* **113**, 9978 (2000).